



# Shape Optimization of an Asymmetric Airfoil for Low Wind Speed Region having Adjoint-Based Optimization Technique

P. Shinde<sup>1†</sup>, S. S. Ohol<sup>1</sup> and V. K. Tripathi<sup>2</sup>

<sup>1</sup> *Mechanical Engineering Department, College of Engineering Pune, Pune, Maharashtra, 411005, India*

<sup>2</sup> *Mechanical Engineering Department, National Institute of Technology, Agartala, Tripura, 799046, India*

†Corresponding Author Email: [sp18.mech@coep.ac.in](mailto:sp18.mech@coep.ac.in)

(Received July 15, 2022; accepted October 10, 2022)

## ABSTRACT

The land needed to install wind turbines is shrinking as power generation from renewable energy sources increases significantly. A large number of studies are being conducted to maximize the power extraction from wind turbines in areas with low wind speeds. Wind turbine blades play a significant role in utilizing the maximum amount of energy from the wind. The aerodynamic performance of a wind turbine blade depends on the airfoil shape. The shape optimization of an asymmetric S2027 airfoil for a low wind speed region was investigated using the adjoint-based optimization technique. The primary objectives of this study were to maximize the lift coefficient, minimize the drag coefficient, and maximize the lift-to-drag ratio. The optimization is based on the adjoint method for Reynolds number variation in the range of  $2 \times 10^5$  to  $5 \times 10^5$  and an angle of attack variation from  $0^\circ$  to  $12^\circ$ . A two-dimensional Reynolds–Averaged Navier–Stokes Computational Fluid Dynamics model was created with all the operating parameters and used for optimization. The aerodynamic performance was validated experimentally. For each optimization function, approximately 16 shapes were obtained. The aerodynamic performance for each optimized shape was determined under different operating conditions. Different airfoil shapes with a specific chord, leading and trailing edges, and span arrangement was obtained. The drag coefficient was reduced by 2%–30%; the lift coefficient was improved by 2%–35%, and the lift-to-drag ratio was improved up to 40%.

**Keywords:** Airfoil shape optimization; Wind turbine blade; XFOIL; ANSYS Fluent; Numerical Simulation Wind tunnel.

## NOMENCLATURE

C	camber	$V_d$	design variable
c	chord length	$V_{ff}$	flow field variable
$C_d$	coefficient of drag	$\nu_t$	eddy viscosity
$C_l$	coefficient of lift	$x_i, x_j$	spatial coordinates
$C_{max}$	maximum camber of an airfoil	$\epsilon$	rate of dissipation of turbulent kinetic energy
D	drag force	$\alpha$	angle of attack
g	computational grid	$\beta^*, \beta_1, \beta_2$	equation constant
k	turbulence kinetic energy	$\sigma_{k1}, \sigma_{k2}, \sigma_{\omega 1}$	
L	lift force	$\sigma_{\omega 2}, \gamma_1, \gamma_2$	
R	flow field	$\frac{\partial}{\partial t}$	Eulerian time derivative
Re	Reynolds number	$\rho$	density of the fluid
t	thickness of the airfoil	$\omega$	specific rate of dissipation
$T_{max}$	maximum thickness of an airfoil	$\mu$	viscosity
$u_i$	time derivative of velocity within a flow	$\mu_t$	viscosity in the RANS region
$V_c$	Lagrangian multiplier vector	$\tau_{ij}$	stress tensor

## 1. INTRODUCTION

Improvements in the airfoil design increase the effectiveness of wind turbines. Various researchers have optimized the airfoil shape in wind turbine blades to improve the production and reduce the cost of energy (Chen and Wang 2018; Fuglsang and Bak 2004; Wang *et al.* 2015)

Various optimization methods have been used to improve the design of the airfoil from the initial stage to final manufacture. Researchers have optimized airfoils based on different objective functions and constraints using different tools and methods (Sharma *et al.* 2020). Aerodynamic shape optimization using computational fluid dynamics has been used for a long time.

Class shape transformation (CST) parameterization (Liang and Li 2018), parameterization (Della Vecchia *et al.* 2014; Fuglsang and Bak 2004), genetic algorithm (Bedon *et al.* 2016; Liang and Li 2018; Mukesh *et al.* 2014; Ram *et al.* 2019), adjoint method (Diwakar *et al.* 2010; Srinath and Mittal 2010), pressure-load inverse method (Henriques *et al.* 2009), and neural networks (Mortazavi *et al.* 2015) have been adopted by researchers. Because airfoil shape optimization requires numerous design parameters, the gradient-based technique is utilized to attain the optimum shape using the objective functions. The gradient-based optimization method is based on using distinct computational methods, such as finite difference and adjoint methods. Adjoint-based optimization requires less computation time to obtain the cost function gradient than the finite difference method. Adjoint-based optimization can determine the gradient in a single cycle without depending on the design variables (Carpentieri *et al.* 2007; Wang *et al.* 2019).

Adjoint-based optimization is considered more efficient when handling the number of variables (Gomes and Palacios 2020; Othmer 2014; Schramm *et al.* 2018). Adjoint-based optimization can be used for both shape and topology optimizations. In a shape-optimization process using an adjoint method, the computational field varies at each optimization cycle via remeshing (Karpouzias and De Villiers 2014).

There is a growing demand for efficient systems to generate energy from alternate sources (Kang and Park 2013).

Airfoil shape optimization has been carried out primarily for high Reynolds (Re) number applications, and studies are lacking for wind turbine applications. The objective functions and variables considered in previous studies are primarily for applications that do not consider wind-turbine applications. The objective of the current analysis is to optimize the profile of the S2027 airfoil using an adjoint method for variation in Re from  $2 \times 10^5$  to  $5 \times 10^5$  and angle of attack from  $0^\circ$  to  $12^\circ$ . For optimization, the objective functions considered were the improvements in the lift coefficient, lift-to-drag ratio and reduction in the

drag coefficient. For wind turbine airfoil optimization, the flow is considered time-dependent, and real-valued functions are based on over-period-averaged aerodynamic factors. The optimized shapes were analyzed using an X-foil to evaluate the performance of each optimized airfoil with a varying range of input parameters. Streamline-upwind and pressure-stabilized Petrov-Galerkin (SUPG and PSPG) stabilization methods have been applied (Srinath and Mittal 2010; Tezduyar *et al.* 1992).

The research work presented in this paper is primarily dependent on urban weather conditions. The data is collected under circumambient conditions. A discrete adjoint solver technique for the shape optimization of an airfoil was implemented. The novelty of the research work is the airfoil (for wind turbine application) shape optimization method (i.e., discrete adjoint solver using less computational time at higher efficiency). The objective functions (i.e.,  $C_l$  maximization,  $C_d$  minimization, and  $L/D$  maximization) are used while varying the Re number (within a certain range) and at different angles of attack. The modified airfoil shape can work in urban weather conditions. This research is a first step toward minimizing the use of land to generate power using wind turbines.

## 2. DISCRETE ADJOINT BASED OPTIMIZATION

For aerodynamic optimization the discrete adjoint approach was used to solve the flow equations around the surface of the airfoil. The equations are obtained using a set of discrete field equations with the direct application of control theory (Nadarajah and Jameson 2000).

The wind turbine operates for an extensive range of Re numbers. The performance of wind turbines varies as the range of Re number changes owing to fluctuations in turbulence, vibrational forces, airfoil surface roughness, etc. (Chen and Wang 2018). In this analysis, the adjoint approach, along with the CFD simulation, was used for shape optimization. Figure 1 shows the procedure for the present analysis and validation approach adopted for the shape optimization of an airfoil to reduce the computational time.

### 2.1. Numerical Aerodynamic Simulation Governing Equations

Using an advanced computation facility, the Navier-Stokes equation can accurately define the fluid motion without any subdivision based on the viscosity, compressibility, and speed of flows. The Navier-Stokes equations are the governing equations for CFD simulations. For turbulence in fluid flows, the equations are averaged, leading to Reynolds averaged Navier-Stokes equations (RANS) (Halila *et al.* 2020; Malone *et al.* 1991). Modelling the Reynolds stress tensor is essential for the mathematical explanation of the RANS equations. The RANS can be written as (Liang and Li 2018):

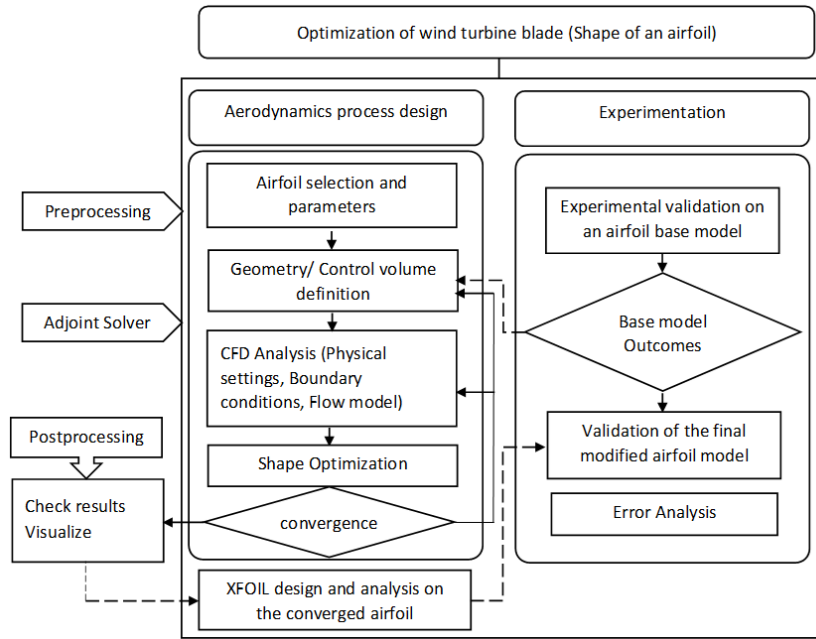


**Fig. 1. Shape optimization strategy.**

$$\frac{\partial u_i}{\partial x_i} = 0, \quad (1)$$

$$\frac{\partial u_i}{\partial t} + \bar{u}_j \frac{\partial \bar{u}_i}{\partial x_j} = -\frac{1}{\rho} \frac{\partial \bar{p}}{\partial x_i} + \vartheta \frac{\partial^2 u_i}{\partial x_j^2} - u_j' \frac{\partial u_i'}{\partial x_j} + f_i \quad (2)$$

Original k- $\omega$  model can be given as:

$$\begin{aligned} \frac{\partial}{\partial t} + u_i \frac{\partial}{\partial x_i} (\rho k) &= \tau_{ij} \frac{\partial u_i}{\partial x_j} - \beta^* \rho \omega k + \\ \frac{\partial}{\partial x_j} \left[ (\mu + \sigma_{k1} \mu_t) \frac{\partial k}{\partial x_j} \right] \end{aligned} \quad (3)$$

$$\begin{aligned} \frac{\partial}{\partial t} + u_i \frac{\partial}{\partial x_i} (\rho \omega) &= \frac{\gamma_1}{v_t} \tau_{ij} \frac{\partial u_i}{\partial x_j} - \beta_1 \rho \omega^2 + \\ \frac{\partial}{\partial x_j} \left[ (\mu + \sigma_{\omega 1} \mu_t) \frac{\partial \omega}{\partial x_j} \right] \end{aligned} \quad (4)$$

Transformed k- $\varepsilon$  model can be written as:

$$\begin{aligned} \frac{\partial}{\partial t} + u_i \frac{\partial}{\partial x_i} (\rho k) &= \tau_{ij} \frac{\partial u_i}{\partial x_j} - \beta^* \rho \omega k + \\ \frac{\partial}{\partial x_j} \left[ (\mu + \sigma_{k2} \mu_t) \frac{\partial k}{\partial x_j} \right] \end{aligned} \quad (5)$$

$$\begin{aligned} \frac{\partial}{\partial t} + u_i \frac{\partial}{\partial x_i} (\rho \omega) &= \frac{\gamma_2}{v_t} \tau_{ij} \frac{\partial u_i}{\partial x_j} - \beta_2 \rho \omega^2 + \\ \frac{\partial}{\partial x_j} \left[ (\mu + \sigma_{\omega 2} \mu_t) \frac{\partial \omega}{\partial x_j} \right] + 2\rho \sigma_{\omega 2} \frac{1}{\omega} \frac{\partial k}{\partial x_j} \frac{\partial \omega}{\partial x_j} \end{aligned} \quad (6)$$

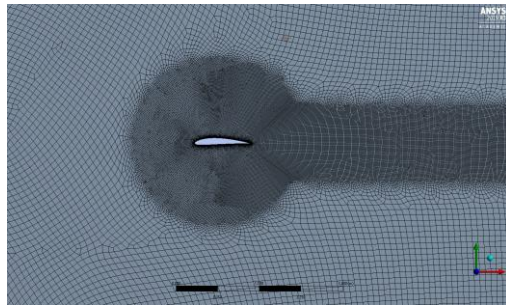
The analysis was based on time-dependent, two-dimensional (2D) RANS equations. Menter developed a shear stress transport model (SST) (Menter 1994), which can be combined with closed and far-field regions. For modelling turbulent flow, the two-equation eddy viscosity (SST k- $\omega$ ) model can be applied with higher accuracy and efficiency. It syndicates the recompenses of both standard k- $\omega$  and k- $\varepsilon$  models by associated functions. The second-order upwind of the discretization along with the pressure velocity-coupled SIMPLEC method was adopted for the

analysis. For the simulation procedure, the finite-volume, education-licensed CFD software ANSYS was used.

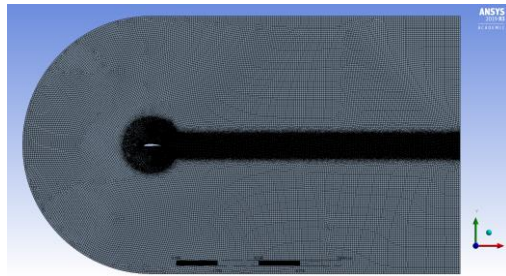
### 2.1.1. Grid generation and grid dependence test for Numerical Analysis of an Airfoil"

Quadratic elements were used for grid generation. Figure 2 shows a 2-dimensional generated grid system. The grid size was refined with a matched convergence criterion at different flow situations near the airfoil, whereas the refinement decreased as the distance from the airfoil increased. The C-shape, 2D computational domain has been generated as it has been adopted by various researchers (He *et al.* 2016; Mortazavi *et al.* 2015). The initial grid generation was performed for the S2027 airfoil with a Re number of  $2 \times 10^5$  and an angle of attack of  $0^\circ$ – $12^\circ$ . The inlet, top and bottom, and outlet boundaries of the enclosed domain are approximately 20, 16, and 30 times that of the airfoil chord, respectively. The enclosed domain is sufficiently far from the airfoil to neglect the boundary effect on the airfoil. The grid generated was approximately  $1.14 \times 10^5$ . The  $y^+$  value was kept near 0.6 for a better degree of fineness in the wall region.

For the analysis of grid dependence, both lift and drag are the two variables (objective functions) that are considered. The variation of both variables for the S2027 airfoil with respect to the angle of attack (design variable) with variations from  $0^\circ$  to  $12^\circ$  is found at a different number of grids. It was found that if the number of grids is more than  $1.14 \times 10^5$ , both variables have the same variation with respect to the angle of attack. Figure 3 shows that this is because of the independence of the grid at and above  $1.14 \times 10^5$ . Therefore, for the present analysis,  $1.14 \times 10^5$  grids were conveniently adopted for further analysis.

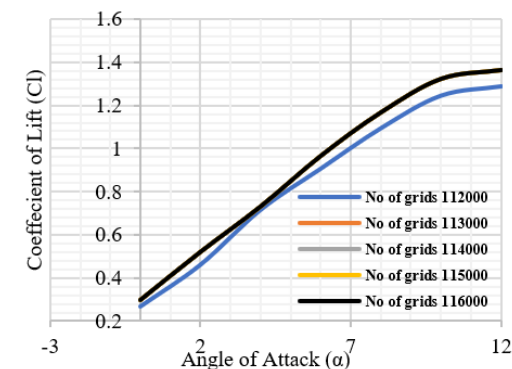


(a)

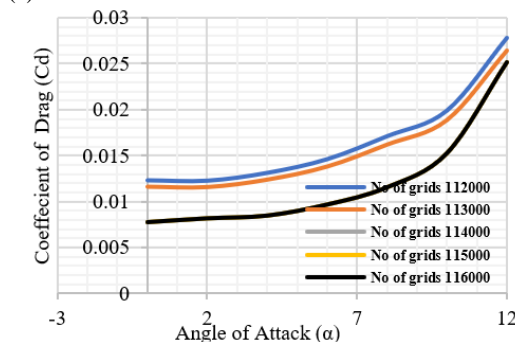


(b)

**Fig. 2. Generated grid system (a) Refined boundary of airfoil and (b) Meshed model of C-sectional 2D computational domain.**



(a)



(b)

**Fig. 3. Coefficient (a) lift and (b) drag variation concerning angle of attack with varied number of grids.**

### 2.1.2. Inlet and outlet boundary conditions during Airfoil shape optimization

The inlet, upper, and lower borders were established as the velocity inlet boundary conditions. The outlet boundary was established using the pressure outlet

boundary conditions. The outlet was at a constant atmospheric pressure. The outer geometry of the airfoil was established as a no-slip wall. The stream velocity was zero at the airfoil boundaries. The residual limit of convergence was considered as  $10^{-6}$ . The wind inlet velocities are varied in such a way that the Re number varied from  $2 \times 10^5$  to  $5 \times 10^5$ , with inlet velocities of 3.3, 4.95, 6.6, and 8.25 m/s, respectively. The mean air fluctuation percentage and turbulent viscosity ratio are set at 6% and 9%, respectively.

## 2.2 Experimental Validation of the Base Airfoil and an Optimized Airfoil

The CFD results must be validated prior to the optimization process. For validation, both XFOIL and experimental analyses were carried out. The results were compared with the base model of the S2027 airfoil. The CFD was performed using ANSYS Fluent to obtain precision in the results. The validation of the CFD results is important for carefully scrutinizing the boundary conditions and variables.

### 2.2.1 Experimental assessment

For the experimental analysis, testing was conducted in an open-type wind tunnel (Fig. 4). The main duct had a cross-section of  $300 \text{ mm} \times 300 \text{ mm}$  and a length of 1000 mm. The tunnel blower provides an air speed of 2–30 m/s. The lift and drag forces were measured using a 0–20 kg beam load cell. Two pitot tubes (a 5/16" and a micro-0–20 mm pitot tube) and a 0–50 mm WC inclined manometer were installed in the system for setting and correcting the flow velocities, as listed in Table 1.



**Fig. 4. Testing Rig.**

A digital anemometer with a measurement range of 0–30 m/s, two digital channel  $3 \frac{1}{2}$  force indicators

**Table 1 Wind Tunnel Specifications**

Parameters	Specification
Design	Open type wind testing tunnel
Main duct material:	Coating of powder with mild steel
Side glass material:	Perspex sheet of about 8 mm in thickness
Size:	300 mm × 300 mm × 1000 mm
Fan blade	5 blades–Aluminum die cast
Air Velocity (test section)	2–30 m/s
Contraction ratio	9:1
Lift/drag force	0–20 kg beam type load cell
Multi-tube manometer	Height is 300 mm
Anemometer display	Velocity range – 0–30 m/s Digital
Stain gauge balance capacity	two channels a) Force – 0–20 kg for lift b) Force – 0–20 kg for drag
Pressure transducers	Type: Differential Pressure Transducer Standard Accuracy: +/- (0.5% RD + 0.2% FS)
Air length	9.5 m
Pitot tube	5/16"
Inclined Manometer	0–50 mm WC
Speed variation:	10% to 100% by Frequency drive controller Vacon
Make:	400 V; Class VFS7-4037
Mode:	p; 2.1 kW- VFD

and two channel strain gauge balances were used for measurement. An annular-gap-type pressure-regulating valve was used to minimize the interference and stabilize the pressure and flow along the test section of the wind tunnel. Based on the manufacturers' data, there can be a 2.8% error in velocity measurements.

### Airfoil Manufacturing

Additive manufacturing is the most effective method to manufacture an airfoil for wind tunnel testing. Precision in designing a complicated asymmetric airfoil shape can be achieved using this technique. Additionally, it is an inexpensive method to fabricate a model for testing purposes. Post-processing for a smoother surface can be performed to obtain accurate results during tests in a wind tunnel.

To study the pressure distribution, the airfoil was fabricated with 11 pressure points: 6 on the extrados and 5 on the intrados. The diameter of each pressure point was 2 mm. Figure 5 shows a view of the airfoil mounted for testing. Figure 6 shows the

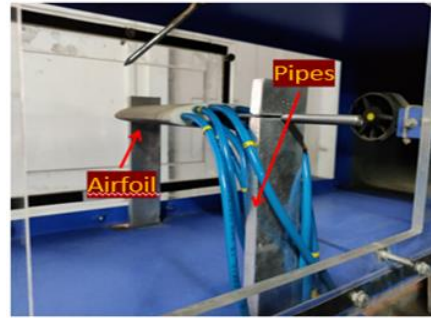


**Fig. 5. Airfoil testing.**

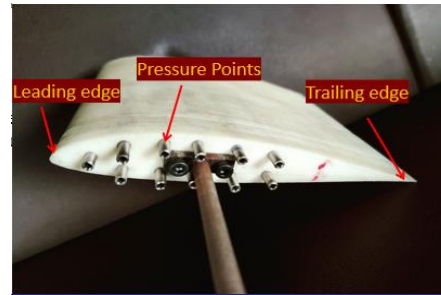


**Fig. 6. Supporting parts of airfoil.**

pressure point, leading edge, and trailing edge of the airfoil. The pressure points were extruded for attachment in order to measure the results. The airfoil had a chord of 150 mm and a span of approximately 150 mm. The first pressure point is situated 15 mm from the leading edge at the x-axis and 10 mm at the y-axis, considering the leading edge at (0,0). The remaining pressure points are at an equal distance of 20 mm from each other, moving from the leading to the trailing edge. Figure 6 shows the location of the pressure points from the leading edge on the chord length (horizontally or in the x-axis) and 4 mm vertically for each of the five pressure points situated near the upper and lower surfaces of the airfoil. Acrylonitrile butadiene styrene with a radius of 2.85 mm was used to fabricate the airfoil. The supporting parts are shown in Fig. 6 attached to the airfoil to support the airfoil during testing.

### 2.2.2 Environment for investigation in XFOIL

The aerodynamic performance of the initial S2027 airfoil was tested using the XFOIL tool at different Re numbers:  $2 \times 10^5$ ,  $3 \times 10^5$ ,  $4 \times 10^5$ , and  $5 \times 10^5$ . About 240-panel nodes were used. NCrit, that is, the free-flow turbulence level, is considered the same as in the CFD analysis. The viscous acceleration is zero.

### 2.2.3 Performance analysis

The results were validated by comparing the experimental and XFOIL outputs for the S2027 airfoil for the coefficients of lift and drag at different Re numbers and angles of attack. A minor difference is observed between the XFOIL, and the experimental results (Fig. 7). With increasing angle of attack the lift and drag forces (Figs. 7(a) and (b)) show similar behavior.

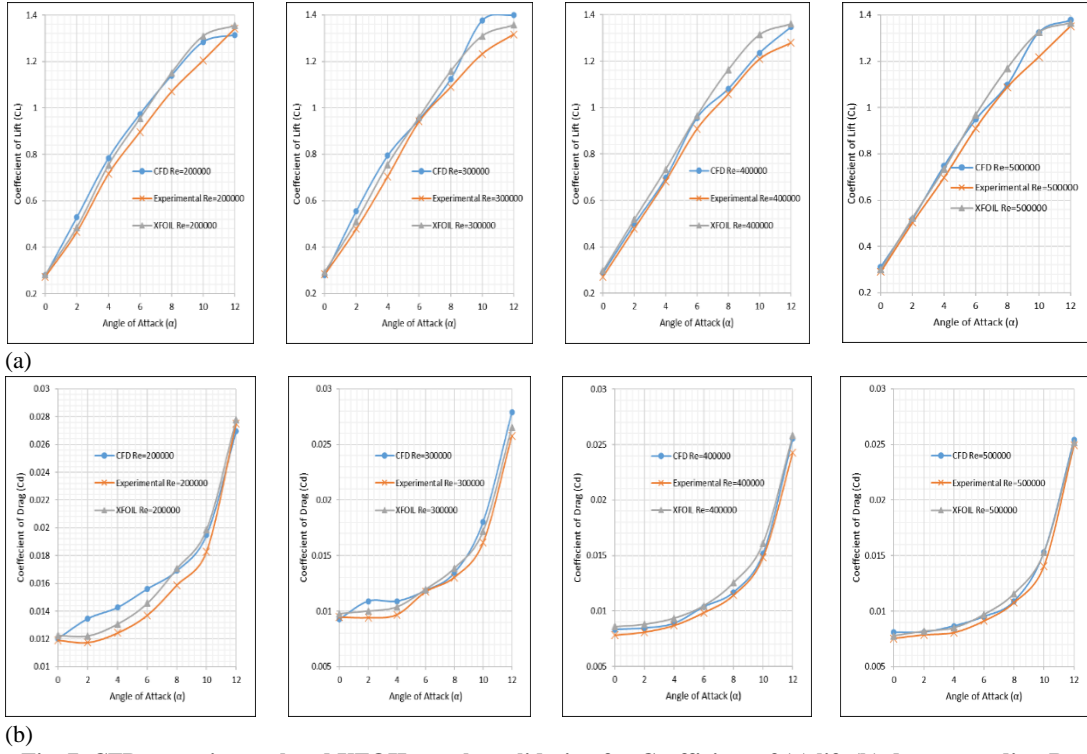


**Fig. 7.** CFD, experimental and XFOIL results validation for Coefficient of (a) lift (b) drag regarding Re number and angle of attack.

It is observed that the forces are in close proximity for the lower value of angle of attack for lift and in the vicinity for the higher value of angle of attack for the drag force. The effect of lift and drag forces for all three methods were within acceptable limits. The error or difference between the results is in the range of -3% to 3%, which can be due to experimental errors. Therefore, this model for CFD can be used for further aerodynamic analysis.

## 2. SHAPE OPTIMIZATION

A deterministic, gradient-based, nonlinear, constraint-based shape optimization method was adopted. The optimization was based on three different objective functions: maximization of lift (at constant drag), drag minimization (at constant lift), and maximization of the lift/drag ratio.

The Lagrange function  $L$  can be described for the objective function and adjoint variables as

$$L(V_d, V_{ff}, g, V_c) = f(V_d, V_{ff}, g) + V_c^T R(V_d, V_{ff}, g) \quad (7)$$

The objective function is represented by  $f(V_d, V_{ff}, g)$ , where  $V_c$ ,  $R$ ,  $V_d$ ,  $V_{ff}$ ,  $g$  are the Lagrangian multiplier vector, flow field, design variable, flow field variables, and computational grid, respectively (M Schramm). The discrete adjoint formulation is given by

$$\frac{dL}{dV_d} = \left( \frac{\partial f}{\partial V_d} + \left[ \frac{\partial g}{\partial V_d} \right]^T \frac{\partial f}{\partial g} \right) + \left[ \frac{\partial V_{ff}}{\partial V_d} \right]^T \left( \frac{\partial f}{\partial V_{ff}} + \left[ \frac{\partial R}{\partial V_{ff}} \right]^T V_c \right) + \left[ \frac{\partial R}{\partial V_d} \right]^T + \left( \left[ \frac{\partial g}{\partial V_d} \right]^T + \left[ \frac{\partial R}{\partial g} \right]^T V_c \right) \quad (8)$$

Because the Lagrangian multiplier vector is basically uninformed, the multiplied terms can be neglected. The term remains

$$\left[ \frac{\partial R}{\partial V_{ff}} \right]^T V_c = - \frac{\partial f}{\partial V_{ff}} \quad (9)$$

The above equation represents the discrete adjoint equation. The objective function to optimize the shape of the airfoil is to

Minimize/Maximize  $F_i = f_i(\alpha, Re)$  ( $i = 1, 2, 3$ ).

Subject to:

$$t \leq T_{max}$$

$$C \leq C_{max}$$

$$Re^{(L)} \leq \text{Reynolds no. (Re)} \leq Re^{(U)}$$

$$\alpha^{(L)} \leq \text{Angle of attack}(\alpha) \leq \alpha^{(U)}$$

where chord length ( $c$ ) is constant,  $F$  is defined as the objective function, and the superscripts  $L$  and  $U$  denote the upper and lower limits of the range of design variables. ‘ $i$ ’ shows the number of objective functions. The objective functions  $F_1$ ,  $F_2$ , and  $F_3$  represent the minimization of the coefficient of drag, the maximization of the lift coefficient, and the maximization of the lift-to-drag ratio, respectively.  $T_{max}$  is the maximum value of thickness, which is 15% at 30%  $c$ , and  $C_{max}$  is the maximum chamber, which is 2.5% at 39%  $c$  of the airfoil. The lower limit of Reynolds no. and the angles of attack were  $2 \times 10^5$  and  $0^\circ$  with increments of  $1 \times 10^5$  and  $4^\circ$ , respectively. The upper limits for both design variables were  $5 \times 10^5$  and  $12^\circ$ , respectively.

Continuous and discrete methods are used for the adjoint solver. In the continuous method, unique relations for partial derivatives are linearized, and adjoints are formed, mathematically discretized, and explained. In the discrete method, the nonlinear stream is linearized completely, with a linear numerical arrangement that is required to answer the adjoint result. For the present analysis, ANSYS Fluent (academic 19.3 R) was used in which a discrete adjoint solver was used. It provided robustness and consistency and evaded the compulsory foisting of the adjoint environment for the continuous method (Petroni *et al.* 2014).

The convergence takes place after many iterations. The rate of change of the selected objective function at each point position on the airfoil surface shows variable sensitivity to particular boundary conditions. After the computation of adjoint shape modification, ANSYS Fluent provides a simultaneous application of adjoint predictions with a volume mesh Morphing optimizer having a smooth surface with numeral control points using Bernstein polynomials. The original S2027 airfoil was used as the baseline. An enclosed control volume for the airfoil is initially defined for the analysis. A network of control points is placed over the meshed surface for mesh morphing to produce smooth changes in the airfoil shape based on Bernstein polynomials. Approximately 25 control points along the chord length and 10 perpendicular points along the chord length were considered as shown in Fig 8(b). The morphing box touches the airfoil boundaries with a complete enclosure.

### 3. RESULTS OF OPTIMIZED PROFILES

During the maximization of the lift coefficient, the drag coefficient was kept constant by the optimizer. Similarly, when the drag coefficient was being minimized the lift coefficient was kept constant. Thus, the reduction and increment were different in both cases. In contrast, the maximization of the L/D ratio causes the optimizer to increase the value of

lift and decrease the value of drag simultaneously, thus obtaining a different value for the L/D ratio. The optimization was performed varying the Re numbers and angles of attack. The Re number was changed from  $2 \times 10^5$  to  $5 \times 10^5$ ; the angle of attack was changed from  $0^\circ$  to  $12^\circ$ . After the adjoint optimization process, the airfoil performance for various series of variables with different angles of attack was obtained using XFOIL and CFD simulation processes.

#### 4.1 Minimization of coefficient of drag

In the optimization process, we determined the optimal shape by considering the minimization of the coefficient of drag at different Re numbers and angles of attack. Figure 8(c) shows the different airfoil profiles obtained with the objective function of minimizing the coefficient of drag for different Re numbers and angles of attack. The shape changes occur primarily on the leading-edge thickness and at the maximum thickness of the airfoil surface.

Figure 9 shows fluctuations of the drag coefficient for each optimized airfoil obtained from a selected range of angles of attack and Reynolds numbers. As the objective function demands minimization of the function value. All the optimized airfoils, as shown in Fig. 8, manifest the minimum drag value for a span of  $0^\circ$  to  $12^\circ$  angle of attack. Observations were made based on the variation in the drag coefficient for minimum and maximum values from 0.000315 to 0.057949, respectively (Fig. 9) for different angles of attack at specific Reynolds numbers. In Fig. 9, for the airfoil profile at a  $12^\circ$  angle of attack and  $Re\ 4 \times 10^5$ , a couloir-type pattern can be observed while increasing the angle of attack from  $-12^\circ$  towards  $0^\circ$ . The aerodynamic behaviour of these airfoils has been investigated for the variation in the lift coefficient and the L/D ratio for the chosen design parameters. Overall, approximately 2%–30% reduction in coefficient drag was observed for all the optimized airfoil shapes.

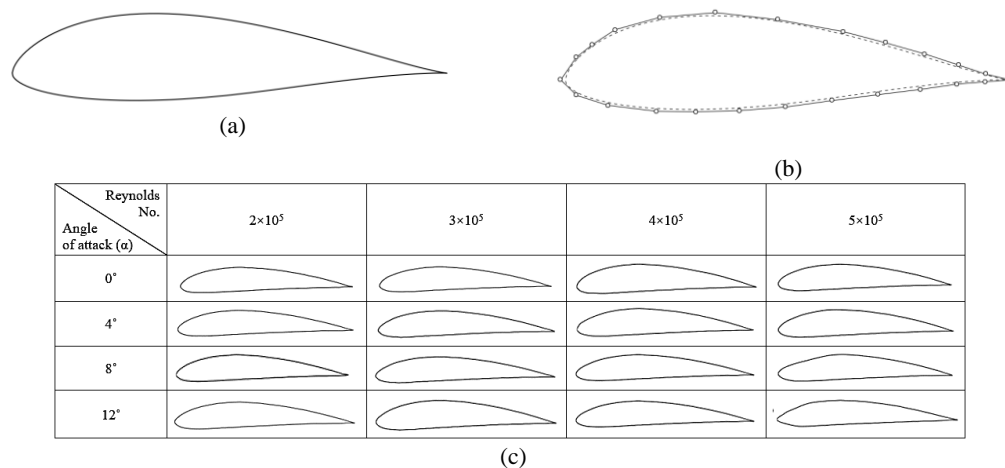
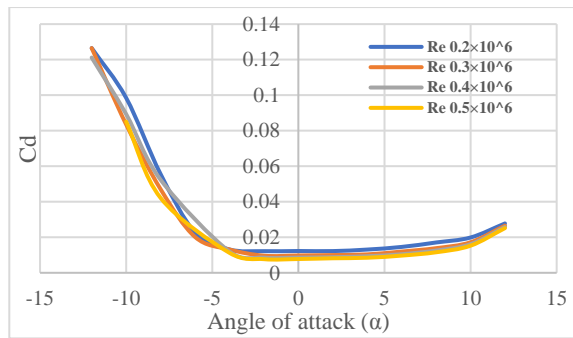
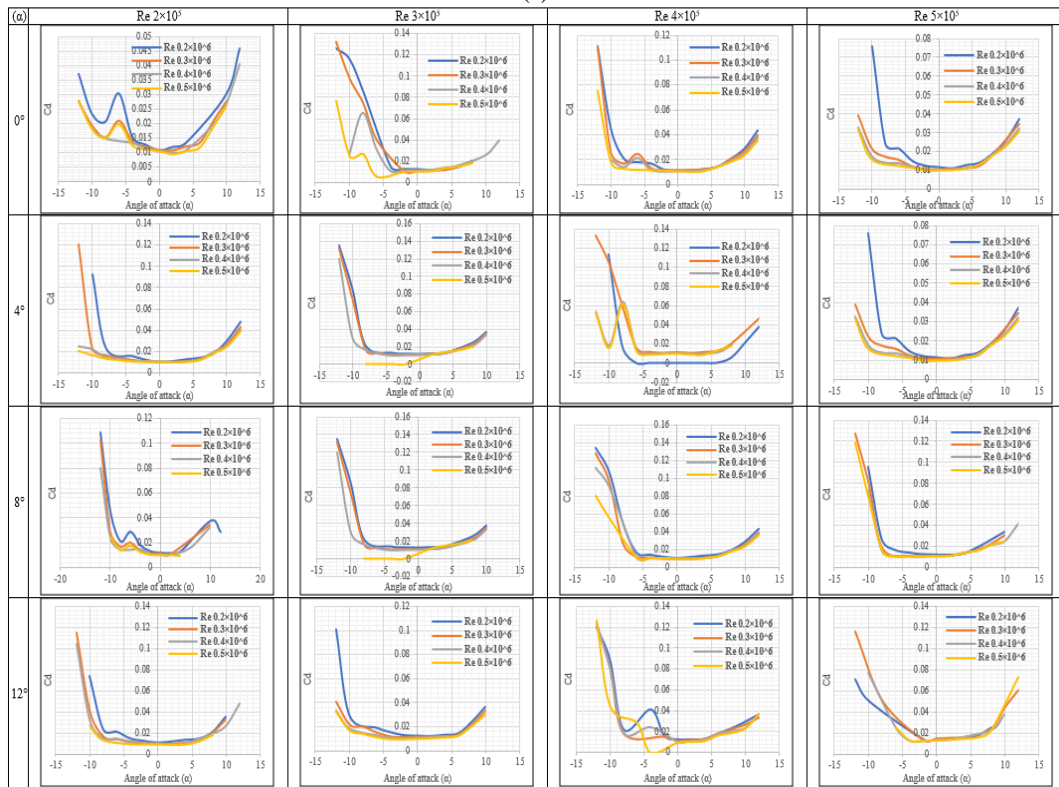


Fig. 8. Airfoil profiles (a) S2027 airfoil shape, (b) Control points on S2027 airfoil, and (c) Profile with the objective function of minimization of coefficient of drag at various Re number and angle of attack.



(a)



(b)

**Fig. 9.** Variation of drag coefficient at different Reynolds no. of the (a) S2027 airfoil, (b) optimized airfoil for an objective function, viz. Minimization of coefficient of drag.

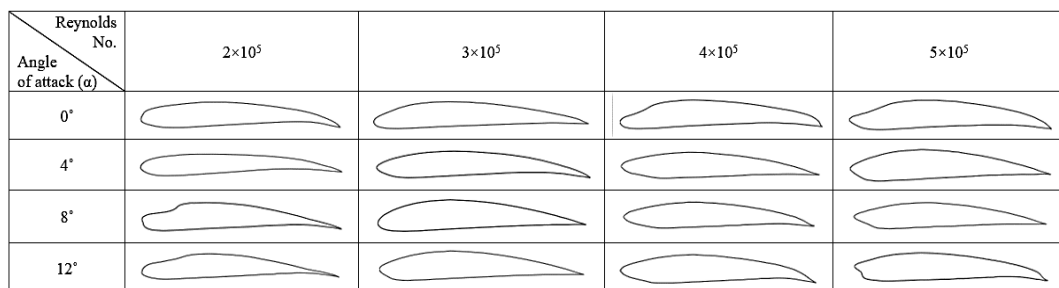


**Fig. 10.** Airfoil profiles with the objective function of maximization of coefficient of lift at different Re numbers and angle of attack.

#### 4.2 Maximization of Coefficient of Lift

This section discusses the optimal shapes obtained for maximization of the lift coefficient. The new airfoil profiles obtained using the objective function are depicted in Fig. 10. The objective function is

maximization of the lift coefficient at various Re numbers, and the angle of attack. The airfoil thickness decreases with a lower Re number, whereas changes in the leading edge are large for higher Re numbers.

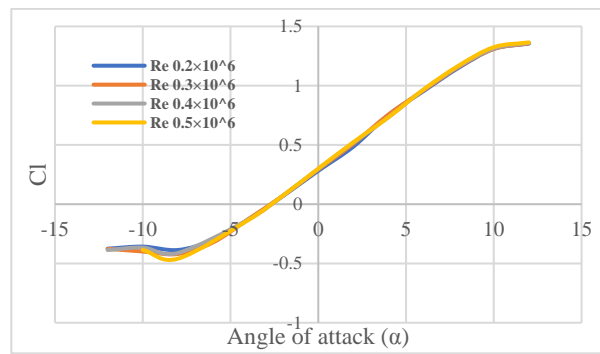
Figure 11 shows the variation in the lift coefficient of the respective airfoil for a wide range of angles of attack at a particular Re number. In Fig. 11, the lift coefficient exhibits fluctuations in the merits of its objective function. The maximum value of the optimized shapes of the airfoils is in the range of 1.5–2. This range shows the smallest deviation in value. There is a visible variation in the graph of the airfoil profile at an angle of attack of 8°, and Re number  $5 \times 10^5$ . This is due to the pressure variation near the leading edge of the optimized airfoil. The implemented optimization process grants an increment of 2% to 35% in lift coefficient.

### 4.3 Maximization of Lift/Drag Ratio

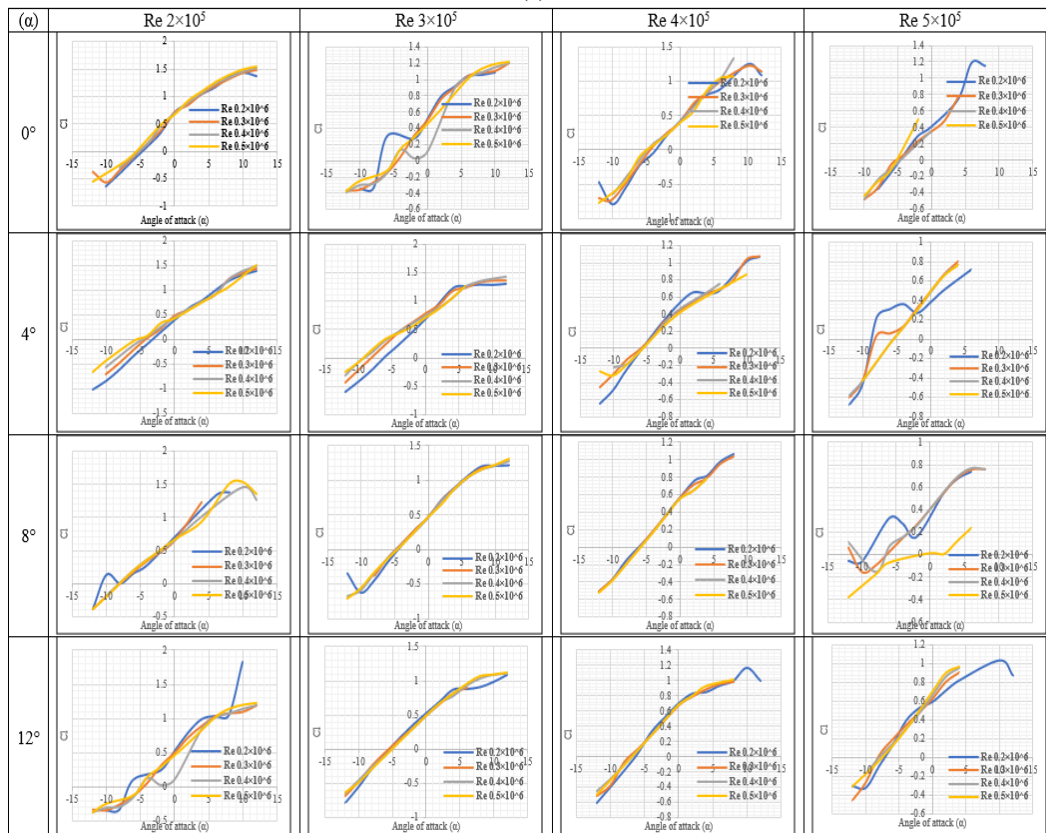
Figure 12 shows the optimal airfoil shapes obtained to maximize the lift-to-drag ratio at different Re number and angles of attack. The airfoil thickness

does not seem to have an effect; however, the leading-edge exhibits different profiles at higher Re numbers, especially at higher angles of attack.

Figure 13 shows the L/D ratio variations of the respective airfoils. It is observed that the crest in the graph for the optimized profile for the L/D ratio for Re number  $5 \times 10^5$  at 0° and 8° shows better performance for a low value of Re number  $0.2 \times 10^6$ . The optimization process shows a maximum lift/drag ratio improvement by 40%. Furthermore, to understand the overall aerodynamic behavior of all the optimized airfoils. The effect of  $C_L$ ,  $C_D$ , and L/D ratio on each selected objective function's optimized shapes of airfoils was performed. All the optimized airfoils showed a satisfactory and acceptable nature for the other goals. The aerodynamic characteristics showed an improvement compared with the base airfoil.



(a)



(b)

**Fig. 11.** Variation of coefficient of lift at different Reynolds no. of the (a) S2027 airfoil and, (b) optimized airfoil for an objective function viz. Maximization of coefficient of lift.

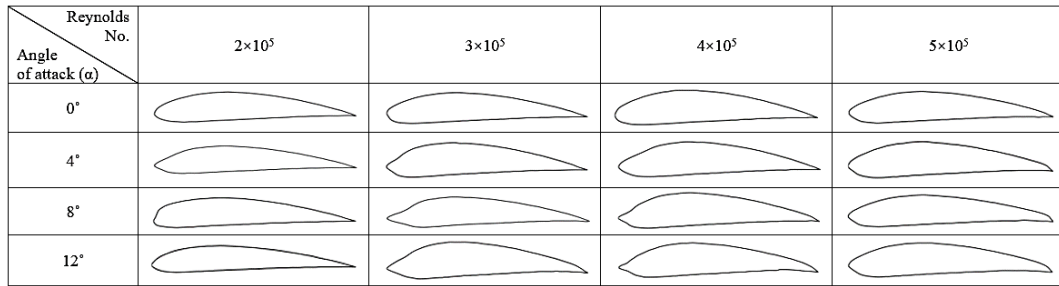
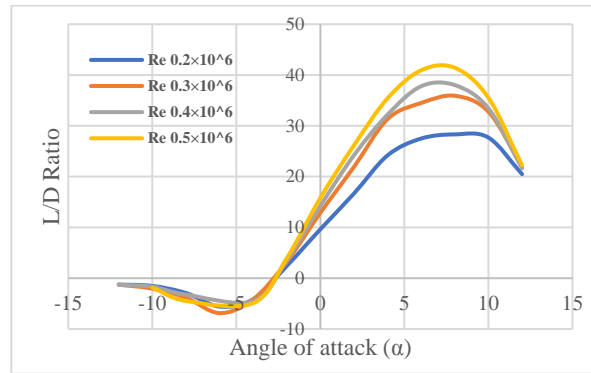
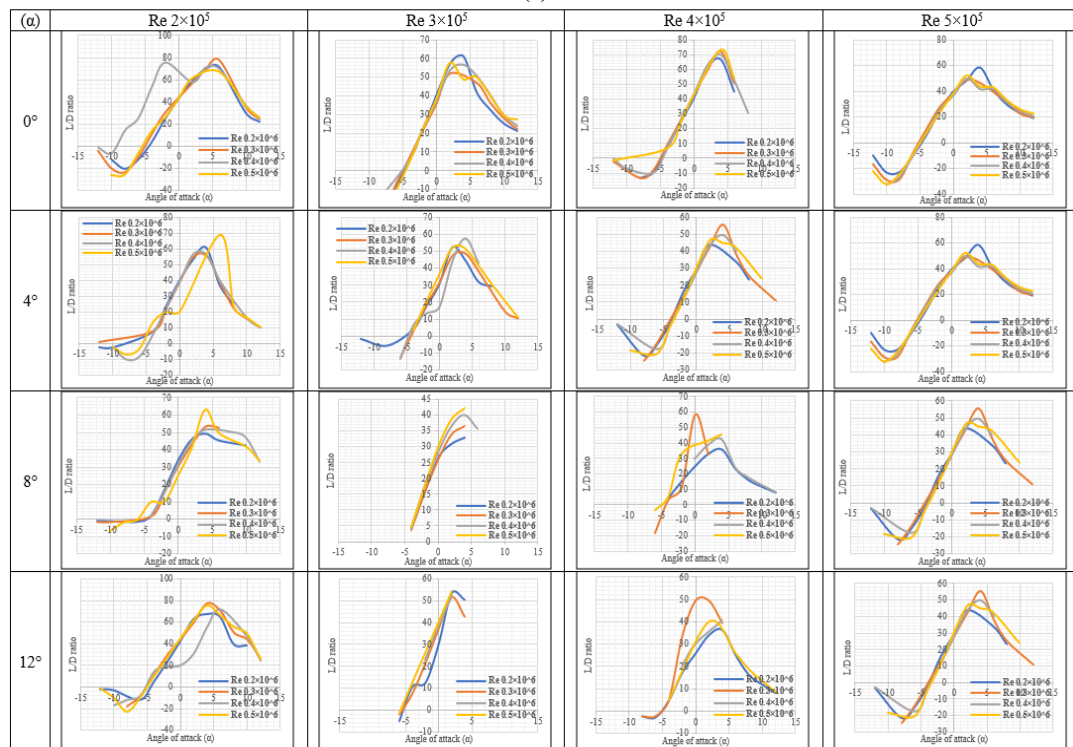


**Fig. 12.** Airfoil profiles with the objective function of maximization of lift/drag ratio for various Re number and angle of attack.



(a)



(b)

**Fig. 13.** Variation of lift to drag ratio at different Reynolds no. of the optimized airfoil for an objective function viz. Maximization of L/D ratio.

#### 4. DISCUSSION AND CONCLUSION

This paper presents the aerodynamic characteristics of an asymmetric S207 airfoil for low-wind-speed regions in urban areas. The aerodynamic behavior

of any airfoil is highly dependent on the two main design parameters, namely, Reynolds number and angle of attack. The selection of Reynolds numbers ranging from  $2 \times 10^5$  to  $5 \times 10^5$  was in accordance with the wind speed in urban areas. A numerical

investigation of the asymmetric S2027 airfoil was performed for a range of angles of attack from 0° to 12°. The results of the numerical investigation were compared with XFOIL and experimental results. Wind tunnel testing was performed on an asymmetric S2027 airfoil to validate the numerical results.

An adjoint based optimization approach is followed to produce a series of new airfoil profiles. A CFD RANS-based model was created to solve both adjoint and fluid flow problems and was validated using experimental and XFOIL results for the primary S2027 airfoil. The objectives for enhancing the aerodynamic characteristics of an airfoil were to maximize the lift coefficient and L/D ratio, and to minimize the drag coefficient. The new series of airfoils contained 48 profiles (refer to Figs. 8, 10, and 12). Each profile is different from the other. Furthermore, each profile was investigated numerically. This study is important as it deals with weather conditions in urban areas. Any of the 48 new airfoil profiles can be used based on the performance requirements in the low-wind-speed region. The study of the aerodynamic characteristics of a new airfoil series is essential for all objectives (refer to Figs. 9, 11, and 13).

1. The numerical analysis method was consistent with the XFOIL and experimental results. A maximum difference of 5% was observed in all the methods used for numerical analysis and experimental validation (refer to Fig. 7). The differences in the results were primarily due to external factors and errors caused by the equipment used for experimental analysis.
2. The new series of 16 airfoils (refer to Fig. 8) for drag coefficient minimization shows a significant reduction in the drag coefficient compared to the base S2027 airfoil. The reduction achieved in the drag coefficient ranged from 2% to 30% (refer to Fig. 9).
3. Maximization of the lift coefficient was accomplished. The lift coefficient's merit increment was up to 2%–35% (refer to Fig. 11). The increment in the lift coefficient was for the new series of 16 airfoils (refer to Fig. 10).
4. Aerodynamic investigation shows acceptable data for 16 profiles (refer to Fig. 12) of the new airfoil series for maximization of the lift-to-drag ratio. The L/D ratio exhibited 40% improved performance than the base S2027 airfoil (refer to Fig. 13).

The performance of the S2027 airfoil, enhanced via shape optimization, showed significant benefits. The enhanced aerodynamic characteristics demonstrated were owing to changes in the shape of the airfoil. The shape changes in the airfoil were at the maximum thickness section; the leading edges were observed with smooth surfaces. Overall, an airfoil shape was introduced for every combination of design parameters. All the airfoil shapes was aerodynamically investigated and exhibited

improved aerodynamic performance in low-wind-speed regions.

## REFERENCES

- Bedon, G., S. De Betta and E. Benini (2016). Performance-optimized airfoil for Darrieus wind turbines. *Renewable Energy* 94, 328–340.
- Carpentieri, G., B. Koren and van M. J. L. Tooren (2007). Adjoint-based aerodynamic shape optimization on unstructured meshes. *Journal of Computational Physics* 224(1), 267–287.
- Chen, J. and Q. Wang (Eds.). (2018). *Wind Turbine Airfoils and Blades*. Science Press Ltd. and Walter de Gruyter GmbH, Beijing/Berlin/Boston.
- Della Vecchia, P., E. Daniele and E. D'Amato (2014). An airfoil shape optimization technique coupling PARSEC parameterization and evolutionary algorithm. *Aerospace Science and Technology* 32(1), 103–110.
- Diwakar, A., D. N. Srinath and S. Mittal (2010). Aerodynamic shape optimization of airfoils in unsteady flow. *CMES - Computer Modeling in Engineering and Sciences* 69(1), 61–89.
- Fuglsang, P. and C. Bak (2004). Development of the Risø wind turbine airfoils. *Wind Energy* 7(2), 145–162.
- Gomes, P. and R. Palacios (2020). Aerodynamic driven multidisciplinary topology optimization of compliant airfoils. *AIAA Scitech 2020 Forum, 1 PartF*, 2117–2130.
- Halila, G. L. O., J. R. R. A. Martins, K. J. Fidkowski (2020). Adjoint-based aerodynamic shape optimization including transition to turbulence effects. *Aerospace Science and Technology* 107, 106243.
- He, X., J. Wang, M. Yang, D. Ma, C. Yan and P. Liu (2016). Numerical simulation of Gurney flap on SFYT15thick airfoil. *Theoretical and Applied Mechanics Letters* 6(6), 286–292.
- Henriques, J. C. C., F. Marques da Silva, A. I. Estanqueiro and L. M. C. Gato (2009). Design of a new urban wind turbine airfoil using a pressure-load inverse method. *Renewable Energy* 34(12), 2728–2734.
- Kang, T. J. and W. G. Park (2013). Numerical investigation of active control for an S809 wind turbine airfoil. *International Journal of Precision Engineering and Manufacturing* 14(6), 1037–1041.
- Karpouzas, G. K. and E. De Villiers (2014). Level-set based topology optimization using the continuous adjoint method. *OPT-i 2014 - 1st International Conference on Engineering and Applied Sciences Optimization*,

*Proceedings June*, 56–74.

- Liang, C. and H. Li (2018). Effects of optimized airfoil on vertical axis wind turbine aerodynamic performance. *Journal of the Brazilian Society of Mechanical Sciences and Engineering* 40(2).
- Nadarajah, S. K. and A. Jameson (2000). A comparison of the continuous and discrete adjoint approach to automatic aerodynamic optimization. *Aerospace Science Meeting and Exhibit*.
- Malone, J. B., J. C. Narramore and L. N. Sankar (1991). Airfoil design method using the Navier-Stokes equations. *Journal of Aircraft* 28(3), 216–224.
- Menter, F. R. (1994). Two-equation eddy-viscosity turbulence models for engineering applications. *AIAA Journal* 32(8), 1598–1605.
- Mortazavi, S. M., M. R. Soltani and H. Motieyan (2015). A Pareto optimal multi-objective optimization for a horizontal axis wind turbine blade airfoil sections utilizing exergy analysis and neural networks. *Journal of Wind Engineering and Industrial Aerodynamics* 136, 62–72.
- Mukesh, R., K. Lingadurai and U. Selvakumar (2014). Airfoil shape optimization using non-traditional optimization technique and its validation. *Journal of King Saud University - Engineering Sciences* 26(2), 191–197.
- Othmer, C. (2014). Adjoint methods for car aerodynamics. *Journal of Mathematics in Industry* 4(1), 1–23.
- Petrone, G., D. C. Hill and M. E. Biancolini (2014). Track by track robust optimization of a F1 front wing using adjoint solutions and radial basis functions. *32nd AIAA Applied Aerodynamics Conference, June*, 1–9.
- Ram, K. R., S. P. Lal and M. R. Ahmed (2019). Design and optimization of airfoils and a 20 kW wind turbine using multi-objective genetic algorithm and HARP\_Opt code. *Renewable Energy*, 56–67.
- Schramm, M., B. Stoevesandt and J. Peinke (2018). Optimization of airfoils using the adjoint approach and the influence of adjoint turbulent viscosity. *Computation* 6(1), 1–23.
- Sharma, P., B. Gupta, M. Pandey, A. K. Sharma and R. Nareliya Mishra (2020). Recent advancements in optimization methods for wind turbine airfoil design: A review. *Materials Today: Proceedings* 47(16), 6556–6563.
- Srinath, D. N. and S. Mittal (2010). Optimal aerodynamic design of airfoils in unsteady viscous flows. *Computer Methods in Applied Mechanics and Engineering* 199(29–32), 1976–1991.
- Tezduyar, T. E., S. Mittal, S. E. Ray and R. Shih (1992). Incompressible flow computations with stabilized bilinear and linear equal-order-interpolation velocity-pressure elements. *Computer Methods in Applied Mechanics and Engineering* 95(2), 221–242.
- Wang, K., S. Yu, Z. Wang, R. Feng and T. Liu (2019). Adjoint-based airfoil optimization with adaptive isogeometric discontinuous Galerkin method. *Computer Methods in Applied Mechanics and Engineering* 344, 602–625.
- Wang, Q., J. Wang, J. Chen, S. Luo and J. Sun (2015). Aerodynamic shape optimized design for wind turbine blade using new airfoil series. *Journal of Mechanical Science and Technology* 29(7), 2871–2882.